PHYSICAL REVIEW D **88,** 023504 (2013)

Constraints on dark matter annihilation by radio observations of M31

A. E. Egorov* and E. Pierpaoli†

Department of Physics and Astronomy, University of Southern California, 3620 McClintock Avenue, SGM 408, Los Angeles, California 90089, USA

(Received 29 March 2013; published 2 July 2013)

We used radio observations of the neighbor galaxy M31 in order to put constraints on the dark matter particle mass and annihilation cross section. Dark matter annihilation in M31 halo produces highly energetic leptons, which emit synchrotron radiation on radio frequencies in the galactic magnetic field. We predicted expected radio fluxes for the two annihilation channels: $\chi\chi \to b\bar{b}$ and $\chi\chi \to \tau^+\tau^-$. We then compared them with available data on the central radio emission of M31 as observed by four radio surveys: VLSS (74 MHz), WENSS (325 MHz), NVSS (1400 MHz), and GB6 (4850 MHz). Assuming a standard Navarro-Frenk-White dark matter density profile and a conservative magnetic field distribution inside the Andromeda galaxy, we find that the thermal relic annihilation cross section or higher $\langle\sigma v\rangle \geq 3 \times 10^{-26}$ cm^3/s are only allowed for weakly interacting massive particle masses greater than $\approx$100 and $\approx$55 GeV for annihilation into $b\bar{b}$ and $\tau^+\tau^-$, respectively. Taking into account potential uncertainties in the distributions of dark matter density and the magnetic field, the mentioned weakly interacting massive particle limiting masses can be as low as 23 GeV for both channels, and as high as 280 and 130 GeV for annihilation into $b\bar{b}$ and $\tau^+\tau^-$, respectively. These mass values exceed the best up-to-date known constraints from Fermi gamma observations: 40 and 19 GeV, respectively [A. Geringer-Sameth and S. M. Koushiappas, Phys. Rev. Lett. **107**, 241303 (2011)]. Precise measurements of the magnetic field in the relevant region and better reconstruction of the dark matter density profile of M31 will be able to reduce the uncertainties of our exclusion limits.

DOI: 10.1103/PhysRevD.88.023504 PACS numbers: 95.35.+d, 95.85.Bh, 98.56.Ne

I. INTRODUCTION

The physical nature of the dark matter (DM) is continuing to be not understood. The most probable candidate for the role of DM is a weakly interacting massive particle (WIMP): a supersymmetric partner of a Standard Model (SM) particle. There are three main approaches in attempts to detect WIMPs: accelerator searches, direct searches, and indirect searches. Although great efforts have been dedicated already to all of these directions, the DM puzzle still seems to be very far from its final and clear solution.

This article is related to the last mentioned search strategy: indirect detection. The idea of indirect detection is based on the opportunity of pair annihilation of WIMPs causing production of different highly energetic SM particles, which eventually decay into stable particles like leptons, protons, and others. These yields may emit electromagnetic radiation through various mechanisms like synchrotron emission, inverse Compton scattering (ICS), etc. in different astrophysical objects. By detecting such radiation we can infer WIMP properties. Since there are evidences of DM existence in any object from dwarf galaxies to largest galaxy clusters, any of these objects are potentially a good target for indirect DM searches. Indirect searches of dark matter have been already extensively exploited considering all wavelength ranges from radio to gamma rays (see [1] for a review). The conventional Lambda cold dark matter model of cosmology suggests a WIMP velocity averaged annihilation cross section $\langle\sigma v\rangle \approx 3 \times 10^{-26}$ cm^3/s, which yields the correct current DM abundance in the Universe in case the DM is thermally produced (see, e.g., [1]). Indirect searches may either lead to the discovery of DM with a given particle annihilation cross section and mass,[1] or constrain the cross section to be below the level of a thermal relic over all plausible ranges of WIMP masses (from several GeV to several TeV). The latter case may imply that, in fact, we do not understand the DM phenomenon in cosmology all that well, and a more sophisticated DM production mechanism is needed.

Currently the most promising direction in indirect detection seems to be related to Fermi searches of the primary gamma emission produced directly by WIMP annihilation (see [3]). At the moment, these constraints are the strongest: they exclude WIMP masses smaller than about 40 and 19 GeV for $b\bar{b}$ and $\tau^+\tau^-$ annihilation channels, respectively, for the standard thermal relic annihilation cross section. While the allowed region of WIMP

*astrotula@gmail.com

†Also at California Institute of Technology, MC 249-17, 1200 East California Blvd, Pasadena, CA 91125, USA. pierpaol@usc.edu

[1]Note that the annihilation cross section at the current epoch can be larger in more general models than the standard thermal value even in the case of thermal production due to effects like Sommerfeld enhancement; see, e.g., [2].

parameters space is gradually shrinking, WIMP masses of hundreds and thousands GeV are still allowed. Indirect searches may allow further insights in the DM phenomenon. Wavelength bands ranging from the radio to the gamma rays and various astrophysical objects may be exploited further to this aim. In this work we studied, in particular, radio observations of the closest big galaxy M31. Relativistic leptons produced by DM annihilation in its halo emit synchrotron radiation on radio frequencies due to Andromeda's magnetic field. Given the size of the galaxy and its DM halo, the strength of its magnetic field and its close distance, large radio fluxes from DM annihilation may be expected from M31. Therefore M31's radio properties may be exploited in order to put strong upper limits on the annihilation cross section. Surprisingly, almost no attempts in this direction have been made in the past: in the literature only few articles can be found dedicated to indirect searches in M31. The most remarkable among them is [4]. These authors obtained some constraints on WIMP parameter space by Cherenkov ground based gamma observations. However, those observations did not have enough sensitivity to probe the relevant region of DM parameters (at least for the conventional WIMPs). Another work, which can be mentioned in the context of WIMP searches in M31 is [5], where the authors studied a detectability of DM minihalos formed around the hypothetical intermediate mass black holes. The conclusion was that such minihalos can be detectable by modern gamma instruments. However, in a contrast with this work, the authors [5] did not aim to put any constraints on the WIMP parameter space. And since the time of these publications [4,5] no significant progress has been made on this object in indirect searches, if we would consider only searches of the ''minimal'' cold dark matter WIMPs.

We computed the expected radio flux due to DM annihilation (Sec. II), and then compared it with available data of radio observations of M31, which allowed us to put upper limits on the annihilation cross section (Sec. III). For comparison with real observations we chose all appropriate radio surveys, which cover a wide range of frequencies: VLSS (74 MHz), WENSS (325 MHz), NVSS (1400 MHz), and GB6 (4850 MHz). The limits obtained can be considered as conservative because we did not make any specific assumptions about the radio emission other than the one from DM in the center of M31, and allowed for an unconstrained contribution from all other unknown backgrounds.

We calculated the constraints for two annihilation channels, specifically the ones annihilating into $b\bar{b}$ and $\tau^+\tau^-$ pairs. We chose these channels among all possibilities because, as explained, e.g., in [6], $b\bar{b}$ and $\tau^+\tau^-$ nearly present the channels with the softest and hardest lepton yields, respectively. Any other case would therefore produce radio fluxes at intermediate levels with respect to these two. In this sense, these can be considered as the two limiting cases.

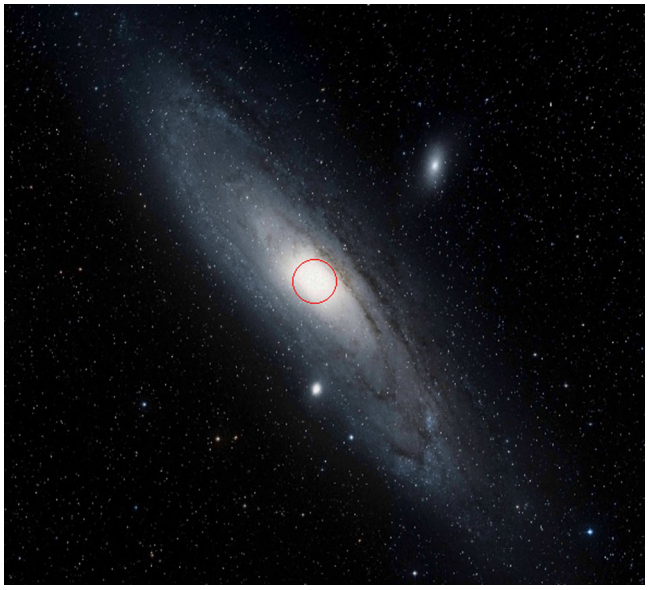

FIG. 1 (color online). Optical image of M31 with the marked ROI, selected for our purposes. Circle radius is $5'$.

In our analysis, we considered only the central part of M31, and specifically the bulge area of a circular shape with the angular radius $\alpha \approx 5'$ around the Galactic center (see Fig. 1). We chose this specific region of interest (ROI) as a target of indirect searches because of the following considerations: (i) the radio quietness of the M31 nucleus, which indicates low contamination in the radio band by other standard astrophysical processes, (ii) the absence of any projected point source inside it, and (iii) sufficient halo size to produce a relevant signal. More details about the ROI choice will be explained below.

Through our paper we adopted the Hubble constant value $H_0 = 71$ km/(s · Mpc), which was taken from the WMAP7 data at [7].

This paper is organized as follows: Sec. II describes computation of the expected radio emission properties due to WIMP annihilation in M31, in Sec. III we derived the actual constraints by comparison of the predicted fluxes with observational data, and Sec. IV summarizes the results of our work.

II. COMPUTING THE RADIO FLUX

A. General theory

In this section we present the procedure for the computation of the radio flux density from the center of M31. We neglected here the potential absorption of radio emission between the source and the observer, since our estimates showed that it occurs at a negligible level (see Appendix A). In the case of an optically transparent emitting medium, the total flux density from our ROI in

M31 can be obtained just by integrating the local medium emissivity $j(\nu, \vec{r})$ over the volume of halo contained in our ROI:

$$S = \frac{\int j(\nu, \vec{r}) dV}{4\pi d^2}, \tag{1}$$

where $d = 785 \pm 25$ kpc is the distance between us and the Andromeda center [8]; $\vec{r}$ is the position vector inside the M31 halo originating in the M31 center. We disregarded here all (small) redshift effects. Then as a next step we needed to compute the local emission coefficient at an arbitrary position in M31 halo $j(\nu, \vec{r})$. The synchrotron emissivity of leptons produced by WIMP annihilation has the form

$$\begin{aligned} j(\nu, \vec{r}) &= \int_{m_e c^2}^{m_\chi c^2} \left(P_{e^+}(E_{e^+}, \nu, \vec{r}) \frac{dn_{e^+}}{dE_{e^+}} dE_{e^+} \right. \\ &\quad \left. + P_{e^-}(E_{e^-}, \nu, \vec{r}) \frac{dn_{e^-}}{dE_{e^-}} dE_{e^-} \right) \\ &= 2 \int_{m_e c^2}^{m_\chi c^2} P_e(E, \nu, \vec{r}) \frac{dn_e}{dE} dE, \end{aligned} \tag{2}$$

where e^+ and e^- represent positrons and electrons, respectively, $P_e(E, \nu, \vec{r})$ is the synchrotron emission power of one lepton with energy E on a frequency ν [measured in erg/(s · Hz) in CGS], and $\frac{dn_e}{dE}$ is the energy distribution of leptons—the number of leptons per unit volume per unit energy range. We assumed electron and positron terms in Eq. (2) to be equal to each other, which is reasonable because these both species behave similarly in all relevant aspects. According to [9]

$$P_e(E, \nu, \vec{r}) = \int_0^\pi d\theta' \pi \sqrt{3} \sin^2\theta' r_e m_e c \nu_0 F\left(\frac{x}{\sin\theta'}\right), \tag{3}$$

where

$$\begin{cases} r_e = \frac{e^2}{m_e c^2}, \\ x = \frac{2\nu}{3\nu_0 \gamma^2}\left(1 + \left(\frac{\gamma \nu_{\rm pl}}{\nu}\right)^2\right)^{3/2}, \\ \nu_0(\vec{r}) = \frac{eB(\vec{r})}{2\pi m_e c}, \\ \nu_{\rm pl} = \sqrt{\frac{e^2 n}{\pi m_e}} - \text{plasma frequency of ambient plasma}, \\ F(t) \approx 1.25(648)^{1/12} t^{1/3} e^{-t} - \text{synchrotron spectrum}, \\ \gamma = \frac{E}{m_e c^2} - \text{lepton Lorentz-factor}. \end{cases} \tag{4}$$

This set of formulas describes the synchrotron power of a lepton in a magnetic field $B(\vec{r})$ in the presence of an ambient plasma with concentration n. Integration over θ' in Eq. (3) represents the averaging over all possible random angles between a lepton's velocity and magnetic field.

In order to proceed with our computation of the radio flux expected, we needed to derive the energy distribution $\frac{dn_e}{dE}$. For this purpose we applied the standard diffusion equation:

$$\frac{\partial}{\partial t}\frac{dn_e}{dE} = \nabla\left(D\nabla\frac{dn_e}{dE}\right) + \frac{\partial}{\partial E}\left(b(E, \vec{r})\frac{dn_e}{dE}\right) + q_e(E, r), \tag{5}$$

where D is the spatial diffusion coefficient, $b(E, \vec{r})$ is the energy loss rate for a lepton through various energy dissipation mechanisms (measured in the units of energy per time), $q_e(E, r)$ is the source function—how many electrons (or positrons—but only one of these two species) are produced by WIMP annihilation per unit time per unit volume per unit energy range. We can simplify this equation, assuming the stationary limit $\frac{\partial}{\partial t} = 0$, as commonly done for the diffusion of DM annihilation products in galaxies and clusters (see, e.g., [10]). Another useful simplification is the absence of the spatial diffusion of annihilation products, which will make the first term in the rhs vanish. We investigated the validity of such an assumption by comparing the characteristic diffusion length of newly injected leptons with the size of our ROI and concluded that it could be done without significant effect on our results (see Appendix B for details). With these two simplifications we can easily solve the diffusion equation:

$$\frac{dn_e}{dE}(E, \vec{r}) = \frac{1}{b(E, \vec{r})} \int_E^{m_\chi c^2} q_e(E', r) dE'. \tag{6}$$

At this point we should specify the functions $b(E, \vec{r})$ and $q_e(E, r)$. The energy loss rate $b(E, \vec{r})$ is constituted mainly by four different cooling processes: ICS emission, synchrotron emission, bremsstrahlung, and Coulomb scattering:

$$b(E, \vec{r}) = b_{\rm ICS} + b_{\rm sync} + b_{\rm brem} + b_{\rm Col}. \tag{7}$$

Using previous results presented in the literature [1,9,11] we constructed each of these four terms, respectively, as follows:

$$b_{\rm ICS} = 0.76 \frac{U_{\rm ph}}{1\ \text{eV} \cdot \text{cm}^{-3}} \left(\frac{E}{1\ \text{GeV}}\right)^2; \tag{8}$$

here, and in other loss terms, numerical prefactors like 0.76 follow from the exact analytical computation of the corresponding loss rate for a lepton. $U_{\rm ph}$ denotes the total energy density of radiation at relevant locations. For the Galactic center region it is constituted mainly by star light photons. We substituted for this quantity the fixed value $U_{\rm ph} = 8\ \text{eV} \cdot \text{cm}^{-3}$, which is quoted in [1] as a characteristic value for the Milky Way (MW) center.

$$b_{\rm sync} = 0.025 \left(\frac{B(\vec{r})}{1\ \mu\text{G}}\right)^2 \left(\frac{E}{1\ \text{GeV}}\right)^2, \tag{9}$$

$$b_{\rm brem} = 4.70 \frac{n}{1\ {\rm cm}^{-3}} \frac{E}{1\ {\rm GeV}}, \quad (10)$$

where n denotes the concentration of ambient plasma in ${\rm cm}^{-3}$.[2] For this quantity we also used the constant value $n = 0.1\ {\rm cm}^{-3}$ relying on the results of the study in Ref. [12], where such a plasma concentration was derived as a typical average value for the Galactic center region.

$$b_{\rm Col} = 6.13 \frac{n}{1\ {\rm cm}^{-3}} \left(1 + \frac{1}{75} \log\left(\frac{E}{m_e c^2 n}\right)\right). \quad (11)$$

All loss rates here are measured in the units 10^{-16} GeV/s. For illustrative purposes, we showed in Fig. 2 the energy dependences of each term in Eqs. (8)–(11) over the relevant range of lepton energies. We can clearly see that the synchrotron losses term depends on the location through $B(\vec{r})$. For this reason, we presented $b_{\rm sync}$ in Fig. 2 for three relevant trial locations, which are away from the M31 center by 0, 1, and 2 kpc. More details about $B(\vec{r})$ distribution will be discussed in Sec. II C. In the most general case, the quantities $U_{\rm ph}$ and n depend on $\vec{r}$ as well, indeed. However, at the current level of accuracy of our model we made two simplifying assumptions. First, we assumed constant values for these quantities with conservative choices, and second, we adopted the values for the MW relying on high similarity between these two galaxies.

As for the source function $q_e(E, r)$, it is computed essentially as a product of the number of leptons produced by one WIMP annihilation per unit energy range $\frac{dN_e}{dE}$ and the number of annihilations per unit time per unit volume:

$$q_e(E, r) = \frac{1}{2}\left(\frac{\rho_{\rm DM}(r)}{m_\chi}\right)^2 \langle\sigma v\rangle \frac{dN_e}{dE}, \quad (12)$$

where $\rho_{\rm DM}(r)$ is the local DM density, $\langle\sigma v\rangle$ is thermally averaged annihilation cross section, and m_χ is the WIMP mass. Annihilation yields of leptons $\frac{dN_e}{dE}$ for two necessary channels $\chi\chi \to b\bar{b}$, $\tau^+\tau^-$ were taken from Ref. [13]. A detailed description of this resource is presented in [14]. We took the precomputed annihilation yields from this resource in their last version, which includes electroweak corrections. The importance of these corrections for a yields computation was justified in [15]. Inclusion of electroweak corrections leads to slightly different secondary lepton yields from annihilation into primary products with different polarizations: left- or right-polarized tau leptons, transversely or longitudinally polarized W bosons, etc. But as practice showed, the difference in the final radiation flux is very minor due to this splitting. For example, the final flux for the case of the M31 DM halo concentration $c_{100} = 12$, observational frequency $\nu = 74$ MHz, WIMP mass $m_\chi = 100$ GeV, and annihilation into $\tau^+\tau^-$ differs just by $<1\%$ for different polarizations, which is much smaller than other total flux uncertainties presented. That is why we did not further distinguish different polarizations of primary annihilation products.

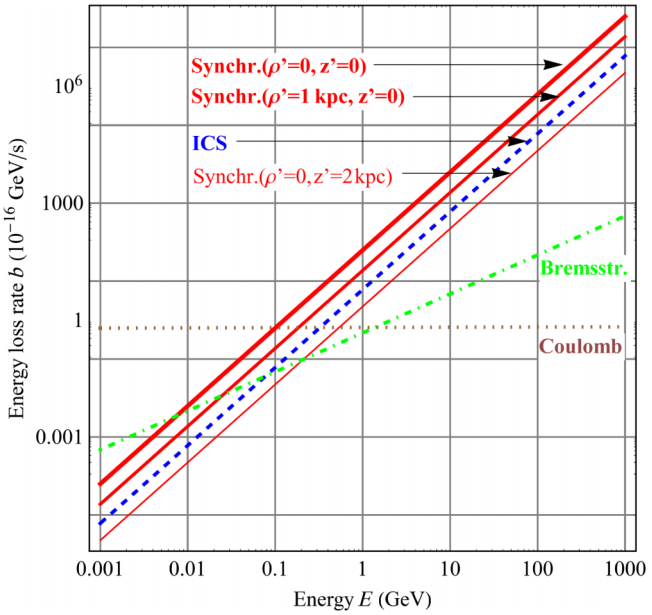

FIG. 2 (color online). The energy dependence of various types of lepton energy losses. Synchrotron losses are shown for three representative locations around the M31 center. For more details see Secs. II A and II C.

For the next step we needed to specify the DM density distribution $\rho_{\rm DM}(r)$, which appears in formula (12). The next subsection is dedicated to the DM density profile derivation.

B. DM density distribution

As a model of DM density distribution $\rho_{\rm DM}(r)$, in M31 halo we used the standard Navarro-Frenk-White (NFW) profile, firstly introduced in [16] and widely used since that due to its universality. Some other profiles potentially describe a DM distribution in galactic halos even better than NFW—this was demonstrated, e.g., in [17] for the Einasto density profile. However, we did not use any other profiles further, except NFW, due to the following reasons. First, all currently available models of the DM density distribution in M31 were made in the frame of the NFW profile. The second reason is that among all profiles, the NFW yields moderate emission fluxes due to DM annihilation (lower than, e.g., the Moore profile—see [10]), and this makes our constraints conservative with respect to the assumptions on the adopted density profile. Also, the NFW profile is specified by only two free parameters, while a larger number of parameters is required by some other

[2]This loss term $b_{\rm brem}$ was presented in another form in Ref. [9]. However, we suspect a mistake at this point in [9], because our verification of this loss rate did not confirm the expression there. For this reason, we use here the expression precisely derived in [11] [formula (6.74) there], which appears to have better justification.

profiles. This choice therefore minimizes the overall number of "degrees of freedom" in our model.

Quantitatively, the DM density distribution of our choice is the following:

$$\rho_{\rm DM}(r) = \begin{cases} \rho_{\rm DM}(r = 50\ {\rm pc}), & \text{if } 0 \le r < 50\ {\rm pc}; \\ \frac{\rho_s}{\frac{r}{r_s}(1+\frac{r}{r_s})^2}, & \text{if } r \ge 50\ {\rm pc}. \end{cases} \quad (13)$$

It presents the exact NFW profile with a minor modification, which can be called as a flat core: we do not extrapolate the density below the radial distance of $r_t = 50$ pc, inside this central region we leave DM density at the constant level of $\rho_{\rm DM}(r = 50\ {\rm pc})$. This choice is motivated by the divergence of the NFW distribution toward the central point of the halo, which prevents us from estimating the DM density reliably in the very central region. The NFW profile provides a reliable density estimate down to the radius ~50 pc for a M31-size halo (see, e.g., Fig. 4 in [18]). That's why in order to be conservative in our computation of the medium emissivity, which depends quadratically on the local DM density, we truncated the NFW profile at $r = r_t = 50$ pc and left the density at smaller radii on the level of $\rho_{\rm DM}(r = 50\ {\rm pc})$. We tested the dependence of our results on the specific arbitrary choice of the truncation radius r_t. This study showed that a decrease (increase) of r_t by a factor of 2 (a factor of 4) produce an increase (decrease) of ≈3% (~10%) in final fluxes, which is far below the overall level of accuracy of our model.

The DM density profile equation (13) is completely defined for a specific halo by two parameters—scaling radius r_s and scaling density ρ_s. Thus, we needed to estimate them for M31. These two parameters are unambiguously linked to another two halo parameters, which are more meaningful—the halo mass M_Δ and its concentration c_Δ. Δ here denotes an overdensity: halo mass M_Δ by definition means the DM halo mass enclosed in the sphere, the average density inside which is equal to $\Delta\rho_{\rm crit}$ with $\rho_{\rm crit} = \frac{3H_0^2}{8\pi G} = 9.5 \times 10^{-30}\ {\rm g \cdot cm^{-3}}$ being the current critical density of the Universe. In our article we used $\Delta = 100$ due to some practical circumstances. However, the parameters of the actual DM density distribution (13) do not depend indeed on a Δ choice. Halo mass and concentration are connected with the NFW profile parameters through the following relations:

$$r_\Delta = \left(\frac{3M_\Delta}{4\pi\Delta\rho_{\rm crit}}\right)^{1/3}, \qquad c_\Delta \equiv \frac{r_\Delta}{r_s}, \qquad M_\Delta = \int_0^{r_\Delta} \rho_{\rm DM}(r) 4\pi r^2 dr. \quad (14)$$

As for the determination of the relevant parameters for M31, we used the results of M_{100} and c_{100} from [8,19]. While these are in a good agreement with each other in determination of M_{100} [$(1.2 \pm 0.3) \times 10^{12} M_\odot$ vs $(0.91 \pm 0.16) \times 10^{12} M_\odot$, respectively], they show a rather big discrepancy in the estimation of c_{100} (the most probable values cited being ≈12 and ≈28, respectively). The expected radiation fluxes from these two concentration values differ by about 1 order of magnitude. This is why we decided to treat these two cases separately. They can be considered as two limiting cases yielding the most conservative constraints for $c_{100} = 12$ and the most optimistic constraints for $c_{100} = 28$.

At this point we were ready to specify the NFW profile by estimation of its two parameters ρ_s, r_s. For the first case $c_{100} = 12$ we took $M_{100} = 1.2 \times 10^{12} M_\odot$ from [8] and obtained ρ_s, r_s by Eq. (14). For the second case $c_{100} = 28$ we did not need to calculate ρ_s, r_s—they were taken directly from Table 2 in [19] as the best-fitting values.

Another potentially relevant question in this subsection is the substructures' contribution in our flux. It is well known that any DM halo contains a lot of small subhalos inside it (see, e.g., [1]). These subhalos are very dense and numerous; that is why they are able to substantially increase the total flux due to DM annihilation from a whole halo—by 10–100 times (see, e.g., [20]). But in our case we can neglect the substructure contribution, because the main part of our expected flux comes from a very central region with a size of about 1 kpc. As can be seen, e.g., in [20], substructures do not survive so close to the center due to tidal disruption, and their contribution to the total expected flux would be negligible at so small radii. Thus, we did not need to include subhalos in our analysis. Moreover, subhalos' presence would only increase the overall flux, so that the constraints obtained here are to be considered conservative.

Thus, at this point we have completely specified the DM density distribution in the M31 halo. Now we can move to the next step—specifying the magnetic field distribution.

C. Magnetic field

The emission due to DM annihilation, which we hope to detect, is generated through the synchrotron mechanism. For synchrotron emission modeling it is crucially important to know the magnetic field strength distribution in our emitting volume. A global axis symmetry of the large spiral galaxy M31 naturally suggests the assumption of a two-parametric magnetic field distribution $B(\rho', z')$, where B depends on the radial distance from the center ρ' in the galactic plane and the vertical height z' above the galactic plane.

As for B dependence on the vertical coordinate z', it's plausible to assume exponential dependence $B \sim \exp(-|z'|/z_0')$ with some scale height z_0'. Such a dependence is commonly used for large spiral galaxies—see, e.g., [21]. In order to consider a reasonable radial dependence of B in the galactic plane we used the findings of [22,23]. In [22], a large-scale magnetic field in the disk plane was measured between radial distances of 6 and 14 kpc. These measurements yielded almost a constant magnetic field over the whole mentioned annular region

of ≈ 7 μG, which is the expected value for galactic discs (see, e.g., [24]). As for the magnetic field strength in the inner region $\rho' < 6$ kpc, we were unable to find reliable data. Some measurements for this region were reported only in [25] and only for two trial locations with poor justification. Besides this information on the central field properties, we can reliably assume probably only one thing—that the field grows toward the center. In such situation we made a decision to introduce the following field distribution (including the vertical dependence part):

$$B(\rho', z') = \left(B_{10} + B_s \exp\left(-\frac{\rho'}{\rho'_0}\right)\right) \exp\left(-\frac{|z'|}{z'_0}\right). \quad (15)$$

Here $B_{10} = 7$ μG—the plateau value observed on $\rho' \approx$ 6–14 kpc. The term $B_s \exp(-\frac{\rho'}{\rho'_0})$ presents an exponentially decreasing central spike with the characteristic radial extent ρ'_0. Of course, such a distribution has a nonphysical plateau extending to infinity $B(\rho' = \infty, z' = 0) = 7$ μG. But this plateau does not matter for our calculations: at distances of tens of kpc DM density becomes very small, and a contribution of these regions to the overall flux is tiny. The distribution in Eq. (15) can be completely specified by two free parameters: the vertical scale height z'_0 and the central field value $B(0, 0) = B_{10} + B_s$. After specifying these two parameters, the radial scale length ρ'_0 becomes automatically set by a smooth connection of the central exponential spike $B_s \exp(-\frac{\rho'}{\rho'_0})$ to the plateau $B(\rho' > 6$ kpc, $z' = 0) \approx 7$ μG.

Now let us discuss the specification of the values of z'_0 and $B(0, 0)$. We estimated the scale height z'_0 using [22,26]. The first mentioned article outlines such a general property of galactic magnetic fields: the scale height z'_0 is typically about 4 times greater than the scale height of a synchrotron emission, which arises from cosmic rays in a whole galaxy volume. The last mentioned synchrotron scale height was reported in [22] for M31 with a value ≈ 0.3 kpc. This would yield $z'_0 \approx 0.3$ kpc $\cdot\, 4 = 1.2$ kpc. Moreover, such a value for z'_0 is confirmed by the authors of [22] on the basis of other independent considerations: they conclude that the minimal expected z'_0 value is not less than ≈ 1 kpc. We therefore chose $z'_0 = 1.2$ kpc for all our calculations. This estimate reflects a conservative choice, since lower values seem to be unrealistic and possible greater values can only increase the final expected flux and, hence, strengthen the final constraints.

As for the second necessary parameter, $B(0, 0)$, the situation is much less certain. As we already mentioned, we found in the literature only one attempt to measure the central field values in M31, [25]. This work reports the total field strengths for the two locations: $B(\rho' \approx 0.3\,\text{kpc}, z' \approx 0) = 15 \pm 3$ μG and $B(\rho' \approx 0.9$ kpc, $z' \approx 0) = 19 \pm 3$ μG. These values were obtained assuming energy equipartition between cosmic ray particles and magnetic fields. Such an assumption, however, has been shown to lead to an underestimation of the magnetic field in similar setting. For example, the authors of [23] explored the central field properties of the MW and derived the stringent lower limit of 50 μG on the field strength based on multiwavelength studies of a cosmic ray emission. At the same time, they mentioned that a simple equipartition assumption implies a central field strength of only ~ 10 μG. As for the upper bound on a central field strength, [23] demonstrates that there is no certainly known value for it. Values of few hundreds μG are mentioned to be absolutely possible.

Considering the possible underestimation of the M31 magnetic field due to the equipartition assumption [25], and the similarity between MW and M31, we chose $B(0, 0) = 50$ μG as the most probable value. However, we performed all our calculations for alternative field values as well (which are considered as less probable) in order to study the dependence of our final results on this model parameter. These alternative less realistic values were chosen to be $B(0, 0) = 15$ μG and $B(0, 0) = 300$ μG. They can be considered as approximate boundaries of the interval where the actual field value lies. The detailed discussion of the final results variation due to uncertainties in $B(0, 0)$ will be done in Sec. III B.

At this point we have completely specified magnetic field distribution. For illustration purposes we showed the density plot of our distribution in Eq. (15) in Fig. 3 for the case of $B(0, 0) = 50$ μG.

The magnetic field distribution in Eq. (15) is written in a cylindrical coordinate system attached to M31. Axes $x'y'$ lie in the M31 disk plane. Another nontrivial step is to

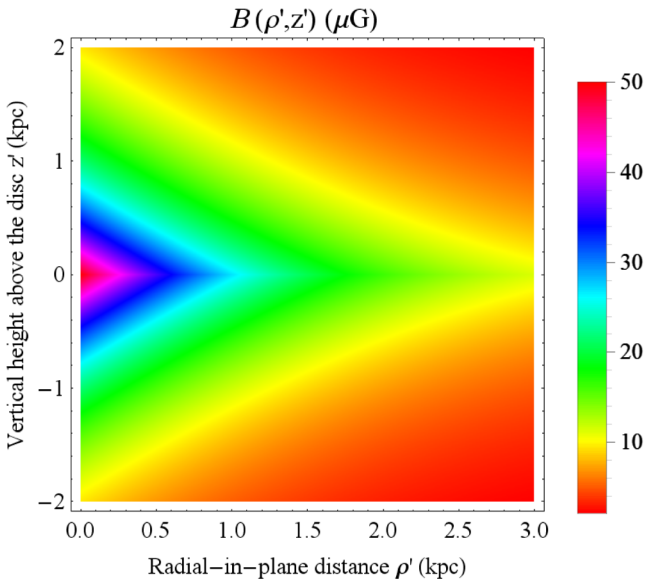

FIG. 3 (color online). Density plot of the magnetic field distribution (15), which was chosen for our computations. Parameter values here correspond to the most probable case with the central field strength $B(0, 0) = 50$ μG. For more details see Sec. II C.

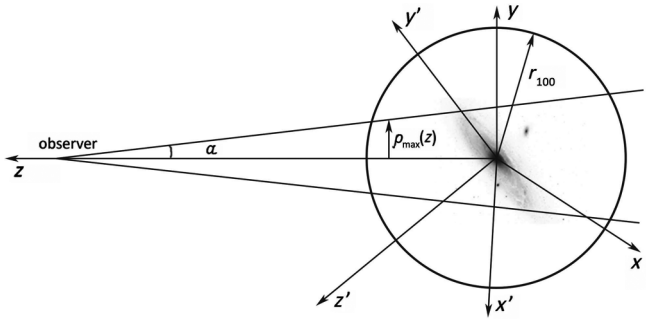

FIG. 4. Two coordinate systems (x, y, z) and (x', y', z'). The plane $x'y'$ is coincident with the M31 disc plane. Integration over the emitting volume is performed in (x, y, z). More details are in Sec. II C.

make a transformation between the coordinate system attached to M31 and the "laboratory" system with the Oz axis pointing from the M31 center to the observer. This is necessary for the flux computation because we are going to perform a numerical integration over the emitting volume along our line of sight, which is coincident with the Oz axis and not coincident with Oz'. The two coordinate systems are shown in Fig. 4. We performed the coordinate transformation $(\rho, \varphi, z) \leftrightarrow (\rho', \varphi', z')$ using the formulas below, which were derived in [27] [formula (6)] for Cartesian coordinates $(x, y, z) \leftrightarrow (x', y', z')$:

$$\begin{cases} x' = -x\sin P + y\cos P, \\ y' = -x\cos P\cos i - y\sin P\cos i - z\sin i, \\ z' = -x\cos P\sin i - y\sin P\sin i + z\cos i, \end{cases} \tag{16}$$

where P and i represent the position angle and axis inclination, respectively, and define the orientation of the M31 disc plane with respect to the sky plane. Following [8], we assumed $P = 38°$, $i = 78°$. From Eq. (16), using relations between cylindrical and Cartesian coordinates it's easy to obtain the one-to-one correspondence $(\rho, \varphi, z) \leftrightarrow (\rho', \varphi', z')$:

$$\begin{cases} \rho' = ((-\rho\cos\varphi\sin P + \rho\sin\varphi\cos P)^2 \\ \qquad + (\rho\cos\varphi\cos P\cos i + \rho\sin\varphi\sin P\cos i + z\sin i)^2)^{\frac{1}{2}}, \\ z' = -\rho\cos\varphi\cos P\sin i - \rho\sin\varphi\sin P\sin i + z\cos i. \end{cases} \tag{17}$$

Finally, we substituted Eq. (17) into Eq. (15) obtaining therefore B as a function of (ρ, φ, z), which allowed us to compute the final flux.

D. Estimated fluxes

A final expected radio flux due to DM annihilation in M31 halo is defined by Eq. (1). In order to compute it we combined all relevant relations (2)–(4), (6)–(15), and (17) and substituted them in Eq. (1). The integration limits for spatial coordinates can be easily figured out from Fig. 4:

$$\begin{cases} 0 \le \rho \le (d - z)\tan\alpha, \\ 0 \le \varphi \le 2\pi, \\ -r_{100} \le z \le r_{100}, \end{cases} \tag{18}$$

where α is the angular radius of our ROI. Figure 5 presents the dependence of the total expected radio flux at $\nu = 74$ MHz on the angular radius of ROI for both selected annihilation channels and three trial WIMP masses: $m_\chi = 10$, 100, and 1000 GeV. Boundaries of every shaded region correspond to the two limiting cases of DM density distribution in the halo, which were discussed in Sec. II B: $c_{100} = 12$ and $c_{100} = 28$. Thus, the actual flux is expected to lie somewhere inside shaded regions. The thick central lines present the algebraic averages between the corresponding boundary curves (fluxes). The flux saturates around $\alpha \approx 5'$ and does not grow significantly at larger radii. We also computed the expected signal-to-noise ratio (SNR) for the same set of parameters and presented it in Fig. 6. Details about noise level computations can be found in Sec. III A. These plots justify our choice of α. Basically, in this choice we are governed by two counteracting effects. On the one hand, Fig. 6 clearly suggests that we use the smallest α possible in order to achieve the best SNR. On the other hand, as discussed in Secs. II B and II C, the accuracy of DM density and magnetic field strength estimates decreases when approaching the central point of the halo. As a matter of fact, we know almost nothing about real distributions of these quantities inside the region of size $\alpha \approx 0.25'$. Hence, our ROI should be much larger than $\approx 0.25'$ in radius in order to encompass a volume where our overall knowledge of the parameters' distribution is precise enough. Based on these considerations, we chose $\alpha = 5'$ as the optimal ROI radius. With such a choice we lose little in SNR; however, we gain in overall reliability of calculations. Also, we cannot increase α any higher than $\sim 5'$ because it will lead to nondesirable capturing of projected point sources.

As an intermediate step of calculations, we decided to study also the contribution of leptons with different energies into the total flux. For this purpose we computed the part of the total flux produced by the leptons with initial energies at production below different thresholds E_m. We spanned the whole possible range of E_m values from the lepton's rest energy to the WIMP's rest energy. The results are presented in Fig. 7 for all four frequencies used. These plots are generated for the most relevant magnetic field model, WIMP mass $m_\chi = 100$ GeV (relevance of this mass scale will be seen in the results section), and the $c_{100} = 12$ halo model. Essentially, we can see in Fig. 7 that the main contribution to the total flux ($\gtrsim 50\%$) for the all frequencies and annihilation channels comes from a relatively narrow window of initial lepton energies between $\sim 0.01 m_\chi c^2$ and $0.1 m_\chi c^2$, or 1 and 10 GeV. This energy window of 1 order of magnitude width is

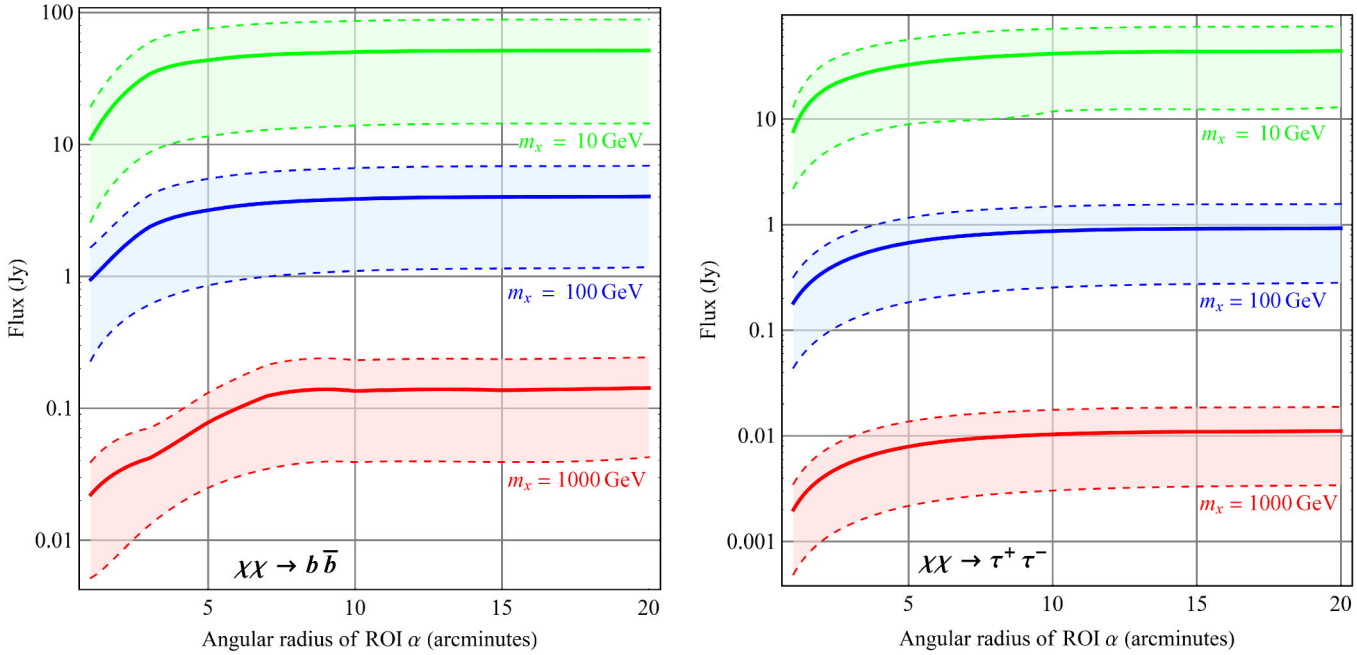

FIG. 5 (color online). The expected radio flux dependence on the angular radius of the ROI. The expected flux lies inside shaded regions. Upper and lower boundaries of these regions correspond to the different halo concentration values $c_{100} = 28$ and $c_{100} = 12$, respectively. Thick central lines present algebraic averages between corresponding limiting cases. Curves are shown for the two annihilation channels $\chi\chi \to b\bar{b}$, $\tau^+\tau^-$, three WIMP masses $m_\chi = 10$, 100, 1000 GeV, and the most probable magnetic field distribution with the central value of 50 μG. The annihilation cross section is $\langle\sigma v\rangle = 3 \times 10^{-26}$ cm^3/s; the observational frequency is $\nu = 74$ MHz. For more details see Sec. II D.

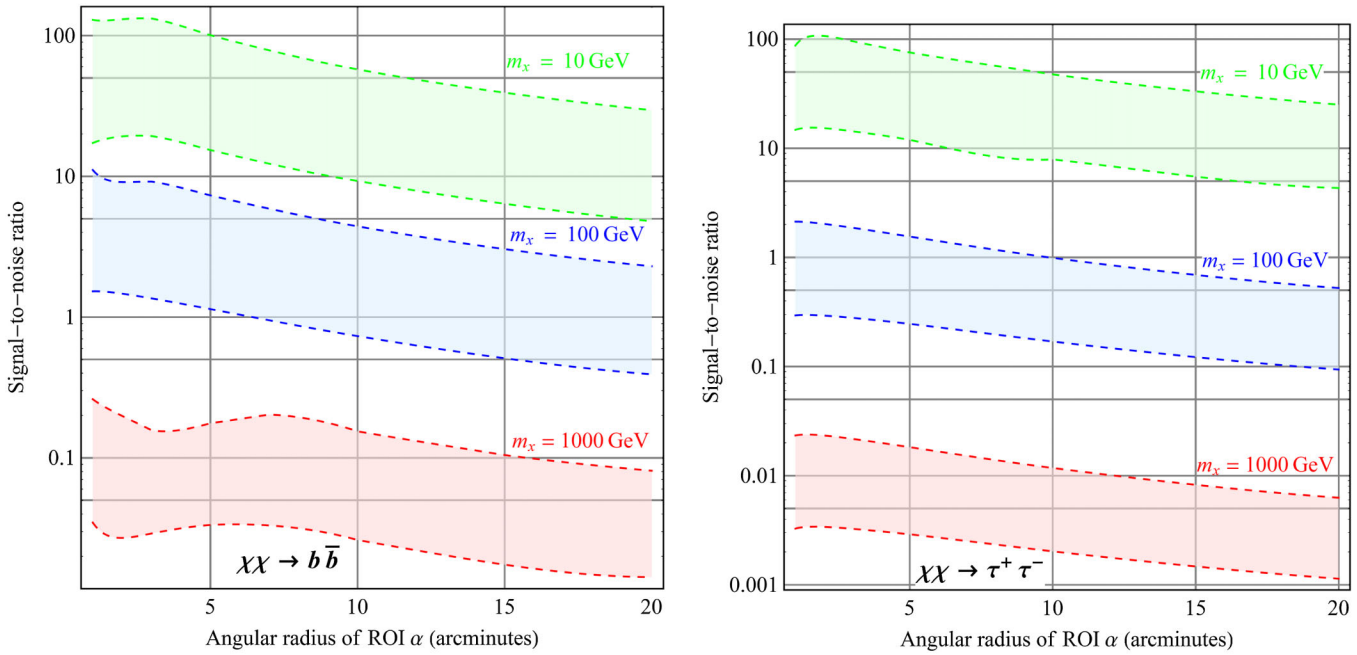

FIG. 6 (color online). The expected SNR dependence on the angular radius of ROI. The expected SNR lies inside shaded regions. Upper and lower boundaries of these regions correspond to different halo concentration values $c_{100} = 28$ and $c_{100} = 12$, respectively. Curves are shown for the two annihilation channels $\chi\chi \to b\bar{b}$, $\tau^+\tau^-$, three WIMP masses $m_\chi = 10$, 100, 1000 GeV, and the most probable magnetic field distribution with the central value of 50 μG. The annihilation cross section is $\langle\sigma v\rangle = 3 \times 10^{-26}$ cm^3/s, the observational frequency is $\nu = 74$ MHz. For more details see Sec. II D.

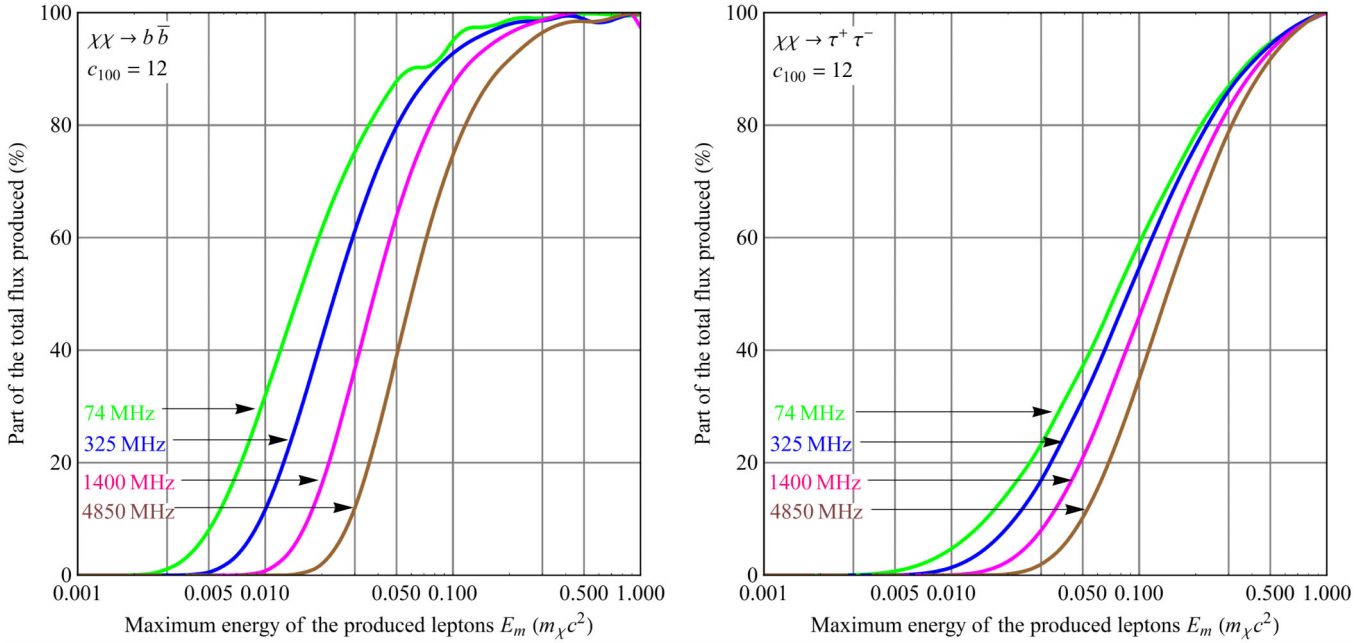

FIG. 7 (color online). The part of total radio flux produced by leptons with energies at production below different thresholds. These illustrations are generated for the following set of parameters: $c_{100} = 12$, $\langle\sigma v\rangle = 3 \times 10^{-26}$ cm^3/s, $B(0, 0) = 50$ μG. The WIMP mass is chosen to be $m_\chi = 100$ GeV, which reflects the most relevant mass scale with respect to the final results, as will be seen below. We can note that the majority of the total flux are produced by leptons with initial energies above $\sim 0.01 m_\chi c^2$. More details are in Sec. II D.

considered to be narrow with respect to the whole energy range of produced leptons between $\sim 10^{-5} m_\chi c^2$ and $1 m_\chi c^2$, which spans more than 5 orders of magnitude. This implies that the most important fraction of the lepton population for our considerations has an energy above ~ 1 GeV. This fact, in turn, means that according to Fig. 2 the main energy loss mechanisms for such a population would be synchrotron and ICS emission. Thus, these

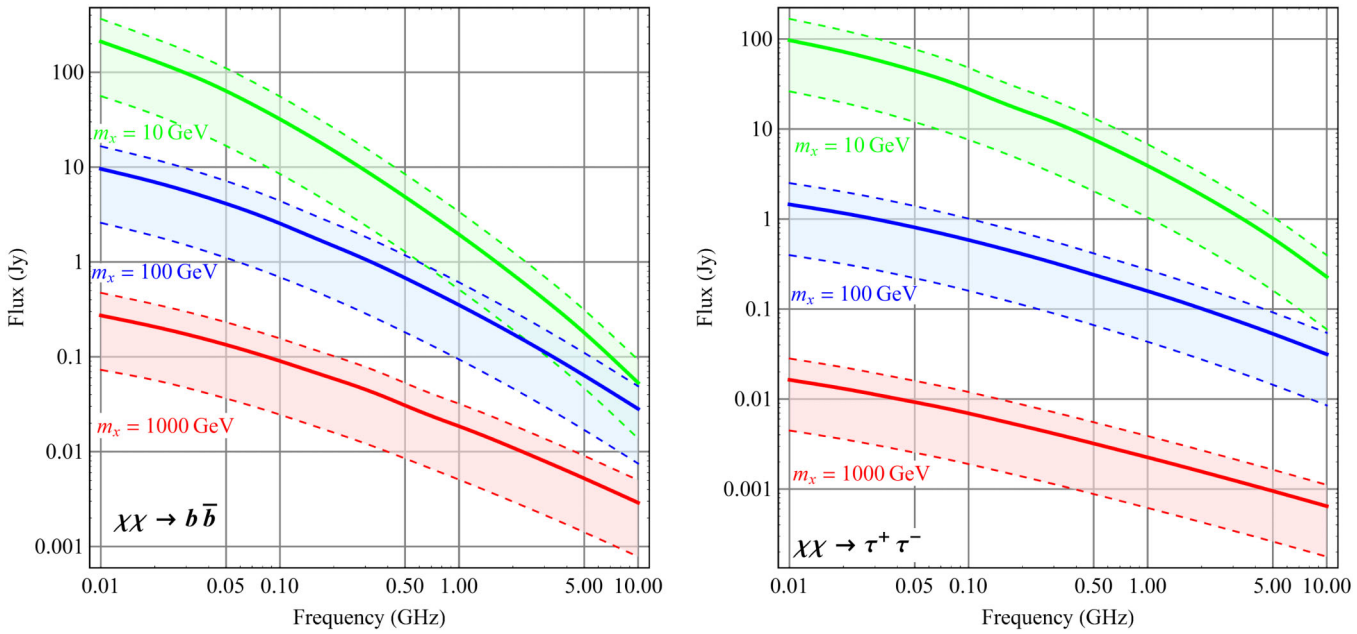

FIG. 8 (color online). The frequency dependence of the expected radio flux for three different WIMP masses and two annihilation channels. ROI radius $\alpha = 5'$; shaded regions reflect uncertainty in the DM density distribution as on the previous plots, $B(0, 0) = 50$ μG, $\langle\sigma v\rangle = 3 \times 10^{-26}$ cm^3/s. More details are in Sec. II D.

kinds of losses dominate in comparison with the other two, bremsstrahlung and Coloumb losses, and play a main role for final results. Meanwhile, it's also useful to note that in the case of the $\tau^+\tau^-$ channel, the total flux is constituted by more energetic leptons than the flux for the $b\bar{b}$ channel, which is in complete agreement with the difference between these two channels mentioned in the Introduction—the $\tau^+\tau^-$ channel produces a harder lepton energy spectrum.

Another important result of our computations is the frequency dependence of radio flux from the M31 halo. These dependencies are shown in Fig. 8 for three different WIMP masses, both annihilation channels, both limiting halo models, and the chosen ROI with $\alpha = 5'$. As a general feature we see, for all cases, a decrease of the radio flux as the frequency increases. The steepness of this decrease is, however, more pronounced for lower WIMP masses. This behavior suggests that we primarily leverage on low frequency observations for obtaining DM constraints. However, the sensitivity of radio surveys typically increases with frequency, partially compensating the effect of the lower signal. There is, therefore, no obvious optimal frequency to be used and that would lead to the strongest constraints possible. For this reason, we opted for radio observations at very different frequencies for actual constraints derivation. This procedure and its results will be described in the next section.

III. OBTAINING CONSTRAINTS ON DM ANNIHILATION

A. Comparison with radio surveys

In order to make a next step on the way to final constraints, we needed to obtain the upper limits on the actually observed radio fluxes from our ROI. A comparison of these upper limits with the expected fluxes computed above immediately provides the upper limits on the annihilation cross section for different values of WIMP masses, since the expected fluxes is directly proportional to $\langle\sigma v\rangle$. For this purpose, we studied many major radio surveys conducted in the past and chose four of them (corresponding frequencies and detailed descriptions are provided in brackets): VLSS (74 MHz [28]), WENSS (325 MHz [29]), NVSS (1400 MHz [30]), and GB6 (4850 MHz [31]). All other surveys were rejected due to either one of the following two reasons: too low resolution of a survey (i.e., the telescope beam size is larger than the ROI size) or not covering the M31 area of the sky. In Table I we outlined the main surveys' parameters, which were collected from [28–31] and then used in calculations. The uncertainties of survey frequencies, caused by finite bandwidth, do not exceed the level of ~4%, and do not affect final results significantly.

Real sky images were viewed and analyzed by the Aladin software, which is described in [32]. The images of our ROI from all four radio surveys are shown in Fig. 9. First, we notice that our ROI does not capture any contaminating point sources. On the last three images (325, 1400, and 4850 MHz) some signal from the M31 center is clearly visible. The 74 MHz image presents essentially noise. For the precise flux upper limit derivations we needed to obtain the measured signal values c_i ($i = 1$–4 denotes different observational frequencies) and the rms (root of mean square or root of dispersion) noise values σ_i for our ROI for all images (we assume Gaussian distributions of noise levels inside a radio telescope beam and inside the ROI). The measured signal values were easily read by the Aladin. As for the rms noise values, we derived from basic principles that they can be estimated as $\sigma_i = \sigma_i^{(b)}\sqrt{N_i} = \sigma_i^{(b)}\frac{\alpha}{\beta_i}$, where N_i are the numbers of beams contained in the ROI, β_i are the angular radii of beams (or half of the FWHM for each survey) and $\sigma_i^{(b)}$ are the rms noises inside a beam for each survey (cited in Table I). Thus, we have obtained both necessary ingredients for a flux upper limit estimation from the ROI—the measured signal values and the rms noise values.

TABLE I. Main parameters of all radio surveys used.

Survey	Frequency (MHz)	Beam diameter or FWHM $2\beta_i$ (arcseconds)	RMS noise level inside the beam $\sigma_i^{(b)}$ (mJy)
VLSS	74	80	100
WENSS	325	82	4.0
NVSS	1400	46	0.5
GB6	4850	240	4.0

Having all the necessary information, we obtained the limiting cross section values for cases of different parameter sets using the following formula for the probability density of the noise values inside our ROI:

$$p_i(n_i = c_i - w_i(\langle\sigma v\rangle)) = \frac{1}{\sqrt{2\pi}\sigma_i}\exp\left(-\frac{(c_i - w_i(\langle\sigma v\rangle))^2}{2\sigma_i^2}\right), \tag{19}$$

where n_i are the noise values inside the ROI, c_i are the measured signal values from the ROI, and $w_i(\langle\sigma v\rangle)$ are the expected signals from WIMP annihilation, which is linearly proportional to an unknown annihilation cross section $\langle\sigma v\rangle$. Here we do not include any background radiation (this question will be further developed in the next section). For our final constraints onto $\langle\sigma v\rangle$ we decided to use 99.73% confidence level, which corresponds to 3σ Gaussian confidence level.

In order to guide intuition on which experiment is the most constraining for a given particle mass, in Fig. 10 we showed our results on the cross section when each frequency is considered individually. There we plotted the constraints obtained at 99.7% confidence level by four different surveys used, for two halo models (described in Sec. II B), two annihilation channels selected $\chi\chi \to b\bar{b}$,

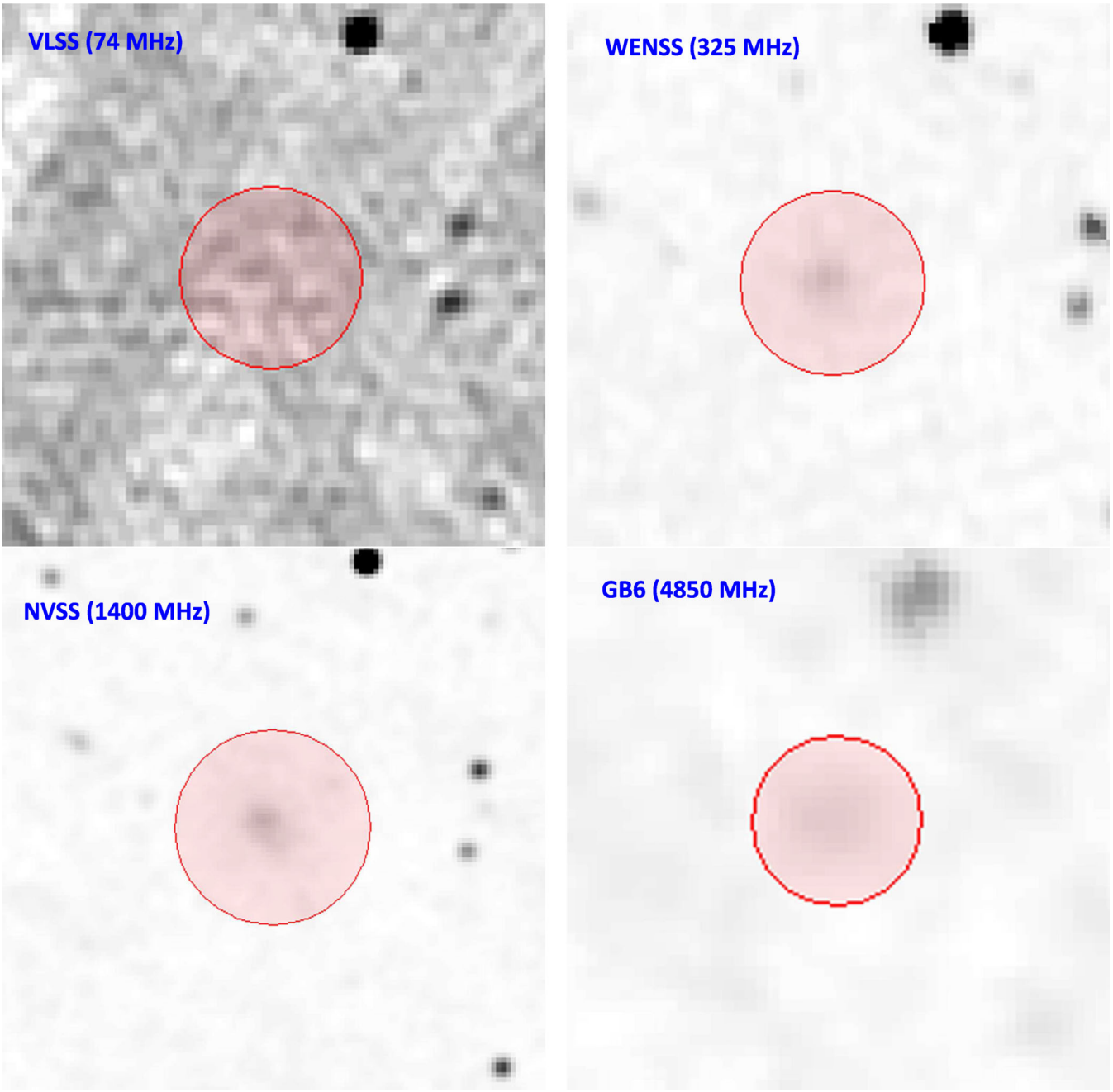

FIG. 9 (color online). Radio images of the M31 central region. Our ROI of 5′ radius is marked by the red circle. Corresponding surveys are commented on each image. We can find noise only on the 74 MHz and significant signals on the other frequencies.

$\tau^+\tau^-$, and the most probable magnetic field distribution with $B(0, 0) = 50\ \mu$G. We spanned the range of WIMP masses between 6 and 1000 GeV and computed the limiting $\langle\sigma v\rangle$ values for a subset of WIMP masses inside this range, interpolating results for mass values in between. The general key properties of our results can be summarized as follows: first of all, different halo models yield very different limiting annihilation cross sections (by about 1 order of magnitude) for all WIMP masses. This reflects the high sensitivity of our results to the halo model assumed. Another noticeable fact is that $\tau^+\tau^-$ annihilation channel appears to be less constrained than the $b\bar{b}$ channel, in complete agreement with the mentioned expectation that harder secondary spectra channels produce a generally lower final radiation flux. It is also interesting to notice that, for different WIMP masses and annihilation channels, the most constraining survey among all the ones considered varies. Therefore, we cannot isolate a specific key frequency or experiment for each plot bearing the role of the most constraining for all WIMP masses—we need to use all experiments together to get the best constraints. And final constraints from the joint analysis will be

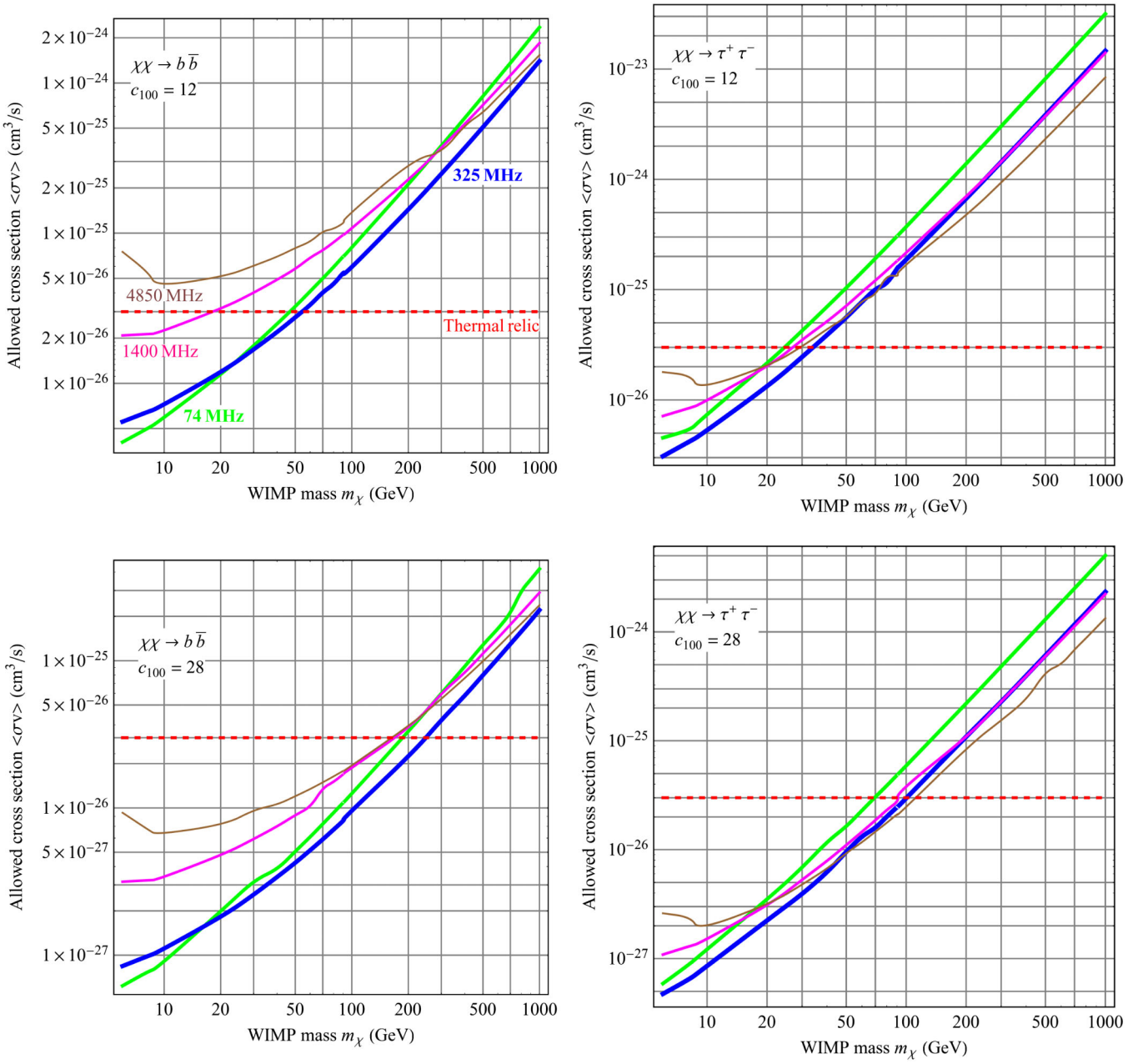

FIG. 10 (color online). All the computed constraints: the WIMP annihilation cross section values above the contours are excluded at 99.7% confidence level. Constraints from different surveys are marked by different colors and thicknesses, which are explained on one of the plots and same for all other plots. Standard thermal relic value $\langle\sigma v\rangle = 3 \times 10^{-26}$ cm^3/s is also shown by the red dashed line. The corresponding halo model and annihilation channel are commented on each plot. No emission sources besides DM are assumed. The magnetic field has the most probable distribution with $B(0, 0) = 50$ μG. For more details see Sec. III A.

gathered in the next section together with analysis of the role of magnetic field uncertainties.

B. Joint analysis and final constraints

Constraints shown in Fig. 10 present exclusion contours from four independent observations. As we can see, these contours lie rather close to each other on each diagram at least for some WIMP masses. Such a situation suggests that we apply a joint likelihood analysis in order to infer combined constraints from all four independent measurements, which we can expect to be better than the constraints taken just considering the exclusion curves in Fig. 10.

Signals other than DM are expected at each frequency. An appropriate modeling of all other astrophysical signals, with their frequency dependence, is necessary in the joint analysis of various frequency maps. We decided to make no assumptions on astrophysical processes other than DM

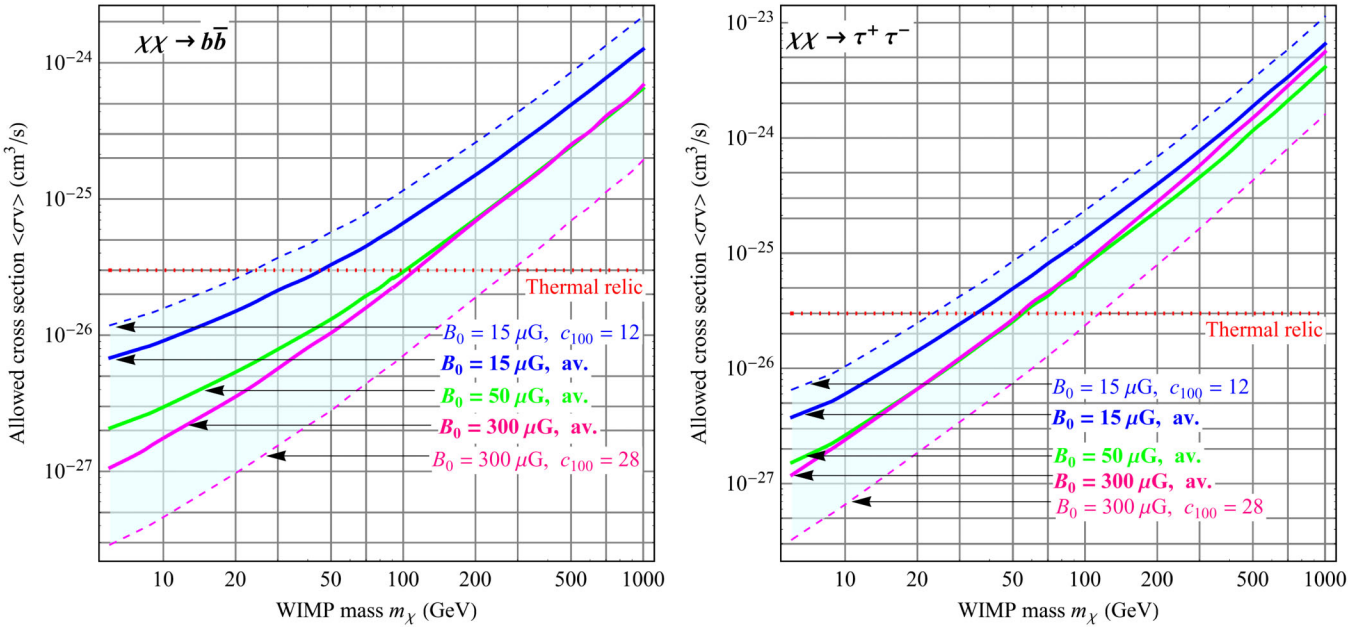

FIG. 11 (color online). Joint constraints including all radio surveys and backgrounds. These plots show all potential uncertainties of both distributions of DM density and magnetic field strength. The dashed contours reflect specific halo models discussed in the text (lines represent 99.7% confidence level). The continuous lines present averages between the exclusions for the corresponding limiting halo models. Different continuous contours illustrate the variation of exclusions due to magnetic field uncertainties. The upper and lower exclusions enclose the shaded regions of all other possible exclusions from the most conservative to the most optimistic ones. More details are in Sec. III B.

annihilation, and simply modeled the total contribution of all other background signals as an *a priori* unconstrained offset uncorrelated between frequency bands. We then performed a standard Bayesian analysis of our data. Following the Bayes theorem (for more details see [33]),

$$p(\vec{\Theta}|\vec{c}) = \frac{p(\vec{c}|\vec{\Theta})p(\vec{\Theta})}{p(\vec{c})}, \tag{20}$$

where the lhs is the desirable probability density distribution for an unknown set of parameters $\vec{\Theta}$ in the case of the observation of data $\vec{c}$, $p(\vec{c}|\vec{\Theta}) \equiv L(\vec{\Theta})$ is the probability density of our observed data $\vec{c}$ for fixed parameters $\vec{\Theta}$ (or likelihood function), $p(\vec{\Theta})$ is the prior probability density of $\vec{\Theta}$, and $p(\vec{c})$ is the marginal likelihood. In our case $\vec{\Theta} = (\langle\sigma v\rangle, s_i)$ is the set of unknown parameters, which we are aiming to infer—annihilation cross section and background radiation fluxes s_i on all four frequencies involved. $\vec{c} = (c_i)$ is the data measured. Then the likelihood function L will have the form

$$p(\vec{c}|\vec{\Theta}) = L(\vec{\Theta}) \sim \prod_{i=1}^{4} \exp\left(-\frac{(c_i - s_i - w_i(\langle\sigma v\rangle))^2}{2\sigma_i^2}\right). \tag{21}$$

This likelihood function presents essentially the product of the independent noise level Gaussian distributions on all frequencies written in terms of the measured and expected fluxes (taking into account that $c_i = s_i + w_i + n_i$). As for $p(\vec{\Theta})$, we made no specific assumptions and chose a constant (flat) prior. The function $p(\vec{c})$ in Eq. (20) does not require specification, since it does not depend on $\vec{\Theta}$ and, hence, plays a role of a normalization constant. After we constructed the five-dimensional density distribution (20) for all five unknown quantities, we needed to integrate Eq. (20) over all possible ranges of noninteresting parameters (marginalization). In our case, we were not interested in background values, so we obtained the distribution for the desired quantity $\langle\sigma v\rangle$ by marginalizing over the background values:

$$\begin{aligned} p(\langle\sigma v\rangle|\vec{c}) &\sim \int L(\vec{\Theta})p(\vec{\Theta})d\vec{s} \\ &= \iint_0^\infty \iint \prod_{i=1}^{4} \exp\left(-\frac{(c_i - s_i - w_i(\langle\sigma v\rangle))^2}{2\sigma_i^2}\right) \\ &\quad \times ds_1 \ldots ds_4, \end{aligned} \tag{22}$$

where we took into account the flat prior. Thus, formula (22) gives us the final probability density distribution for an annihilation cross section combined from all four observations with possible unknown backgrounds included. From this distribution, we easily constructed the final exclusion contours. We presented them for the case of 99.73% confidence level in Figs. 11 and 12, where the allowed area is below the exclusion contours for the corresponding models.

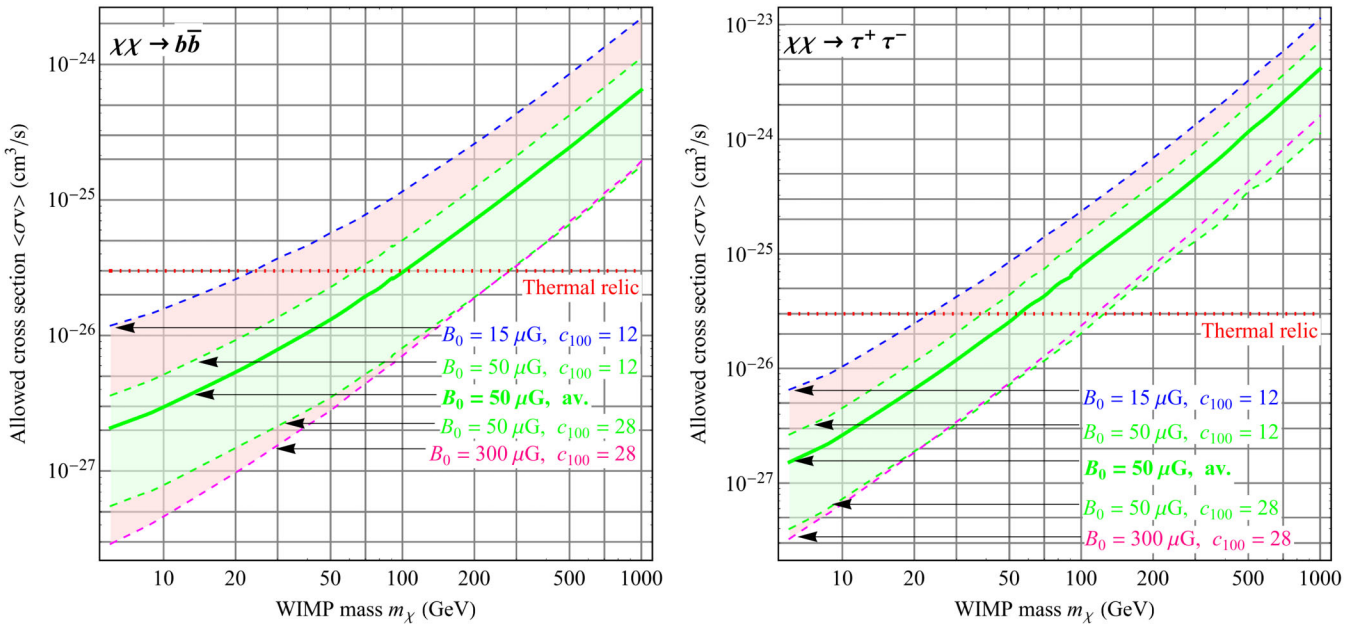

FIG. 12 (color online). Joint constraints obtained. These plots incorporate potential uncertainties of both distributions of DM density and magnetic field strength. The continuous line presents the most realistic exclusion contour, which corresponds to the result of our work on the fiducial case we assumed [average exclusion between those which correspond to the two limiting halo cases and the most realistic magnetic field distribution with $B(0, 0) = 50\ \mu$G]. The shaded area around the continuous contour, which is constrained by the dashed green lines marked as $B_0 = 50\ \mu$G, corresponds to dark halo model uncertainties only. The largest possible shaded region enclosed into the dashed lines, which are the outermost with respect to the continuous contour on each plot, incorporates both uncertainties of the dark halo and magnetic field. For more details see Sec. III B.

We included in our final results possible uncertainties in the magnetic field distribution discussed in Sec. II C. As we outlined there, this distribution is uncertain in two aspects—its vertical scale height z_0' and the central field strength $B(0, 0)$. As for the z_0', our trial runs showed that z_0' variation over all possible values is able to change the final exclusion values of $\langle\sigma v\rangle$ by no more than $\langle\sigma v\rangle^{+5\%}_{-20\%}$ for all possible sets of model parameters. This variation is considerably smaller than the one induced by, e.g., halo model uncertainties, and would suggest less conservative limits. For these reasons, we do not consider it in our final results. However, we cannot treat in this way the second important parameter—$B(0, 0)$, because practice showed significant variation of the final exclusions due to uncertainties in $B(0, 0)$ discussed in Sec. II C. According to this discussion, we expect $B(0, 0) = 50\ \mu$G to be the most probable, but we also consider here $B(0, 0)$ values of $\sim$15 and $\sim$300 μG as limiting cases. We obtained all our final exclusions for these three different magnetic field distributions.

Our results are presented in Figs. 11 and 12. In these figures, the dashed lines represent the specific halo models (either $c_{100} = 12$ or $c_{100} = 28$), while the solid lines correspond to the algebraic averages between the two limiting halo models, for fixed magnetic field values. The two figures show limiting curves for different combinations of the (three) possible magnetic field models and (two) possible halo models. Figure 11 shows more explicitly the dependence on the field strength, while Fig. 12 shows the dependence on the halo model for the reference field strength $B(0, 0) = 50\ \mu$G, and allows us to compare these uncertainties with the ones caused by variation in the magnetic field.

As we can see, annihilation with the standard thermal relic cross section $\langle\sigma v\rangle = 3 \times 10^{-26}$ cm^3/s is excluded

TABLE II. WIMP masses in GeV, below which annihilation with the canonical cross section is excluded, for the different halo and magnetic field models. The most realistic cutoff values are emphasized.

Central field $B(0, 0)$	$c_{100} = 12$, $\chi\chi \to b\bar{b}$	Averaged flux, $\chi\chi \to b\bar{b}$	$c_{100} = 28$, $\chi\chi \to b\bar{b}$	$c_{100} = 12$, $\chi\chi \to \tau^+\tau^-$	Averaged flux, $\chi\chi \to \tau^+\tau^-$	$c_{100} = 28$, $\chi\chi \to \tau^+\tau^-$
15 μG	23	45	160	23	35	88
50 μG	63	*100*	280	39	*55*	130
300 μG	75	110	280	38	53	110

for a significant part of the WIMP mass range. We listed in Table II the precise WIMP mass values for all models considered, below which $\langle\sigma v\rangle$ is less than 3×10^{-26} cm^3/s. These masses were obtained as the contact points between the corresponding exclusions and the thermal relic threshold in Figs. 11 and 12. We can see a significant spread in limiting masses around those which correspond to our preferred model with $B(0, 0) = 50$ μG and the averaged flux between two limiting halo cases. For this most realistic model the WIMP masses that do not allow the standard relic cross section are the ones smaller than 100 and 55 GeV for $b\bar{b}$ and $\tau^+\tau^-$ channels, respectively. In general, these limits were derived with rather conservative assumptions. A discussion of our results and comparison with other studies will be done in the next section.

IV. SUMMARY AND DISCUSSION

In this work, we derived constraints on the WIMP mass and annihilation cross section from radio observations of M31. Annihilating DM in M31 halo produces highly energetic secondary leptons, which, in turn, emit synchrotron radiation due to Andromeda magnetic field. We computed the expected characteristics of this radiation. We first modeled the DM density distribution in M31, using the standard NFW density profile. Previous studies ([8,19], see also [34]) of the M31 halo provide a mass determination, as well as parameters for the fit to the density distribution.

While they agree on the halo mass determination ($M_{100} \approx 10^{12} M_\odot$), they significantly differ in the quoted halo concentration parameter—$c_{100} \approx 12$ vs $c_{100} \approx 28$. We therefore treated these two cases separately and considered them as limiting cases of possible halo models for M31.

As for the modeling of the magnetic field distribution within M31, we used measured values for M31 whenever available, and some extrapolations of MW properties. This is justified by the high similarity between M31 and MW, and also by the much more detailed knowledge we have about the MW. Our reference field distribution is characterized by the 50 μG value of the central field strength and an exponential decline both in vertical and radial-in-plane directions. Then we computed the secondary particle yields from WIMP annihilation using the results of the DarkSUSY package. We neglected the spatial diffusion of the injected leptons, and we calculated expected final fluxes in optically transparent media approximation. We compared these fluxes with available radio observations of M31 spanning a wide range of frequencies: VLSS (74 MHz), WENSS (325 MHz), NVSS (1400 MHz), and GB6 (4850 MHz). This allowed us to derive limits on the cross section $\langle\sigma v\rangle$ as a function of particle mass (ranging from 6 to 1000 GeV). Our analysis is conservative in the sense of the absence of any specific assumptions about a possible radiation other than from DM. The final results are presented in Sec. III in Figs. 11 and 12. We also computed our results for the alternative less probable magnetic field models with the central field values of 15 and 300 μG in order to study the dependence of our final constraints on this model parameter.

Our main result is the exclusion of the possibility of WIMP annihilation with the thermal cross section $\langle\sigma v\rangle = 3 \times 10^{-26}$ cm^3/s or higher for WIMP masses below $\approx$100 GeV ($\approx$55 GeV) for the $b\bar{b}$ ($\tau^+\tau^-$) annihilation channel. However, these estimations are affected by significant uncertainties. Taking into account potential uncertainties in DM density and magnetic field distributions, these limits could be as low as 23 GeV and as high as 280 GeV for the $b\bar{b}$ channel. For annihilation into $\tau^+\tau^-$ these limits, respectively, are 23 and 130 GeV (see Table II).

Our results are comparable with other constraints on WIMP masses derived through other observations. The current best constraints in indirect DM searches were obtained by an analysis of Fermi observations of MW satellites [3]. The reported lowest allowed WIMP masses are 40 and 19 GeV for $b\bar{b}$ and $\tau^+\tau^-$ channels, respectively, for the case of the thermal cross section. When considering 95% systematic errors in the DM distribution within the dwarves, the derived WIMP mass lower limits vary over the ranges 19–240 GeV ($b\bar{b}$) and 13–80 GeV ($\tau^+\tau^-$).

The constraints derived in this work, implying masses above 100 and 55 GeV in order to obtain a relic cross section, are within the range of uncertainties of the current Fermi results. This shows the power of a multifrequency approach in indirect detection: all wavelength ranges may make valuable contributions toward final determinations of allowed parameter ranges. As for other studies dedicated to indirect searches at radio frequencies, we can compare our results with the similar studies for MW [10] and M33 [21]. Our constraints are significantly stronger than the last cited, since the exclusion contours obtained by the authors of [10,21] lie well above the thermal relic value $\langle\sigma v\rangle = 3 \times 10^{-26}$ cm^3/s on the WIMP mass-annihilation cross section plane for any possible WIMP masses ($\langle\sigma v\rangle \lesssim 10^{-24}$ cm^3/s there). Also we can compare our results with the slightly newer work [35] dedicated to the MW gamma and radio constraints. This work reported the relatively stronger exclusions in comparison with, e.g., [10]: $\langle\sigma v\rangle \lesssim 3 \times 10^{-26}$ cm^3/s for the best combinations of parameters (including WIMP mass). However, [35] exclusions are still weaker than ours for M31, as can be seen from Figs. 11 and 12.

We show here, for the first time, that it is possible to constrain the WIMP parameter space significantly employing radio observations of M31. Specifically, while making conservative assumptions, we were able to exclude small WIMP masses for conventional, thermally produced DM. However, the range of higher masses of hundreds GeV is still absolutely allowed and unexplored. This paper presents only the first relatively simple step in a comprehensive analysis of M31, and does not yet include all

potential uncertainties and relevant effects. Particularly, in order to increase an overall level of precision and reliability of our model, it would be necessary to properly introduce the spatial diffusion of annihilation products in our calculations, as this may play some non-negligible role (see Appendix B for an initial estimate). The advantage of the current diffusion-free model resides in its simplicity: our semianalytical results are not affected by large uncertainties related to lepton propagation. This simple model revealed a high constraining potential of M31 in indirect searches. Thus, this first step can be a motivation for a DM community for much more extended investigations of M31. Overall, this work may be expanded in two main directions. First, astrophysical uncertainties can be treated with a more general approach, including further studies of the lepton propagation, magnetic field uncertainties, interstellar radiation field distribution, and others. In addition, while encouraged by current findings, the potential to study this object with other current and upcoming radio telescopes may be explored.

ACKNOWLEDGMENTS

We would like to thank Wendy Lane, the Principal Investigator of the VLSS radio survey, for valuable discussions regarding observational aspects. Also, we are grateful to Jennifer Siegal-Gaskins for generally useful feedback. E. P. acknowledges support from JPL-Planck Subcontract No. 1290790. E. P. and A. E. E. were partially supported by NASA Grant No. NNX07AH59G. We acknowledge the use of the Legacy Archive for Microwave Background Data Analysis (LAMBDA), part of the High Energy Astrophysics Science Archive Center (HEASARC). HEASARC/LAMBDA is a service of the Astrophysics Science Division at the NASA Goddard Space Flight Center [7].

Note added in proof.—While our work was in preparation, the newer study [34] of the M31 dark halo was published. This study reported a quite similar value for the M_{100} and $c_{100} \approx 17$ for the NFW profile. Since the value quoted for the concentration is in between the ones we considered, the implied constraints would lie within our current uncertainty regions for the case of the NFW profile.

APPENDIX A: ABSORPTION ANALYSIS

Here we discuss all potentially relevant mechanisms of absorption of radio emission during its propagation from the M31 center to the observer. We focused only on a potential absorption inside M31 and did not consider possible absorption in MW, because the Andromeda galaxy lies far enough from the galactic plane, and we do not expect any significant absorption in this direction on the sky. In general, inside the Andromeda there are two main agents of interstellar medium relevant for our purposes: a dust and an ionized gas. Among them a dust can be excluded as an absorber rather easily: typically a dust grain size does not exceed 10^{-4} cm (see, e.g., [36]). And the wavelengths of radio emission involved are 10–1000 cm, which is many orders of magnitude larger than grain sizes. In such a case, when a wavelength is much greater than an obstacle size, it is well known that radiation does not interact with obstacles. Thus, we can conclude that a dust does not affect radiation in the considered frequency range.

A situation with the absorption by interstellar plasma is more tricky. Here we can distinguish several possible ways of absorption. First of all, let us check the Langmuir frequency of plasma involved. As is well known, a radiation cannot propagate through plasma if its frequency is less than the Langmuir frequency of the propagation medium. The Langmuir frequency is defined as

$$\nu_{\rm pl} = \frac{\omega_{\rm pl}}{2\pi} = \sqrt{\frac{e^2 n}{\pi m_e}}, \tag{A1}$$

where n is the concentration of plasma electrons which needs to be estimated. For this purpose we used the results of [12], where the gas density distribution was obtained for the central region of MW. Taking into account that MW and M31 are very similar galaxies, we can extrapolate results for MW on M31 staying at the necessary level of accuracy. From [12] we can easily see that the plasma concentration in a Galactic center cannot exceed $n \lesssim 10\ {\rm cm}^{-3}$ in the worst case, which yields $\nu_{\rm pl} \lesssim 30$ kHz. Thus, the Langmuir frequency is much smaller than the observational frequencies of MHz-GHz, which means that the interstellar plasma is transparent with respect to this absorption mechanism.

Another potentially relevant mechanism is a synchrotron self-absorption. Synchrotron emission, generated by relativistic leptons from DM annihilation, can be absorbed by neighbor emitting leptons. In order to estimate the level of this absorption quantitatively we computed the corresponding optical depth along our line of sight, which goes through the M31 center:

$$\tau_{ss} = \int_{\rm los} \alpha_{ss} dl, \tag{A2}$$

where α_{ss} is the synchrotron self-absorption coefficient. We used the derived expression for α_{ss} from [37] [formula (6.50) there]:

$$\alpha_{ss} = -\frac{c^2}{8\pi\nu^2} \int_{m_e c^2}^{m_\chi c^2} dE P_e(E, \nu, \vec{r}) \cdot E^2 \frac{\partial}{\partial E} \times \left(E^{-2} \cdot 2 \frac{dn_e}{dE}(E, \vec{r}) \right), \tag{A3}$$

where $P_e(E, \nu, \vec{r})$ is the synchrotron power of one lepton defined by Eqs. (3) and (4), $\frac{dn_e}{dE}(E, \vec{r})$ is the stationary energy spectrum of emitting leptons of one kind derived by Eq. (6). Then we substituted all relevant values of

the parameters involved. Particularly, for WIMP mass and frequency of observations we used as an example $m_\chi = 100$ GeV and $\nu = 74$ MHz. Such a combination of all parameters yields $\tau_{ss} \sim 10^{-3}$, which means that we can neglect by synchrotron, self-absorption completely and reliably. And this conclusion is valid for all other frequencies used in our work, because α_{ss} decreases with frequency and 74 MHz is the lowest frequency of observations. In general, this conclusion agrees with the results of [6], where the authors solved a similar DM annihilation problem with an application to MW. And they also showed an irrelevance of synchrotron self-absorption on all frequencies.

And the last potential absorption mechanism, which has to be checked, is a free-free absorption by plasma. Here we also estimated the corresponding optical depth:

$$\tau_{ff} = \int_{\text{los}} \alpha_{ff} dl, \tag{A4}$$

where the absorption coefficient α_{ff} was also taken from [37] [formula (5.18b) there]:

$$\alpha_{ff} = 3.7 \times 10^8 T^{-1/2} Z^2 n^2 \nu^{-3} \left(1 - \exp\left(-\frac{h\nu}{kT}\right)\right) g_{ff}, \tag{A5}$$

where n and T are the plasma concentration and temperature, respectively. As for the spatial distribution $n(\vec{r})$, it does not appear to be obtained in the literature for M31. That is why we decided to use such distribution for MW again as an approximation. Taking all relevant information from [12] and assuming $g_{ff} \approx 1$ and $Z = 1$ (hydrogen plasma) we estimated $\tau_{ff} \lesssim 0.01$ in the worst case scenario. Thus, we can see that the free-free absorption is not relevant for our work as well in the first approximation.

Summarizing, in this section we have conducted the detailed analysis of all potentially relevant absorption mechanisms of radio emission generated by DM annihilation. None of these mechanisms achieves a significant level. This conclusion is in agreement with similar studies [6,10] for the MW. Thus, we can ignore any absorption in our analysis without significant loss of accuracy.

APPENDIX B: SPATIAL DIFFUSION OF ANNIHILATION PRODUCTS

Here we study the role of the spatial diffusion of annihilation products in our problem. In order to understand the importance of the spatial diffusion for our final results, we should compare the characteristic distance, which annihilation products travel while they are emitting relevant radiation, with the characteristic size of the emitting region. According to, e.g., [10], the diffusion path traveled by leptons can be calculated as $l_D = \sqrt{D(E)\tau_{\text{loss}}(E)}$, where $D(E)$ is the diffusion coefficient for leptons participating in Eq. (5); $\tau_{\text{loss}}(E)$ is the cooling time of leptons, during which they are emitting the expected radiation and losing their energy until escaping the relevant energy domain. We took the diffusion coefficient $D(E)$ from [10], where it is provided for the MW, and expected to work roughly for the Andromeda galaxy as well:

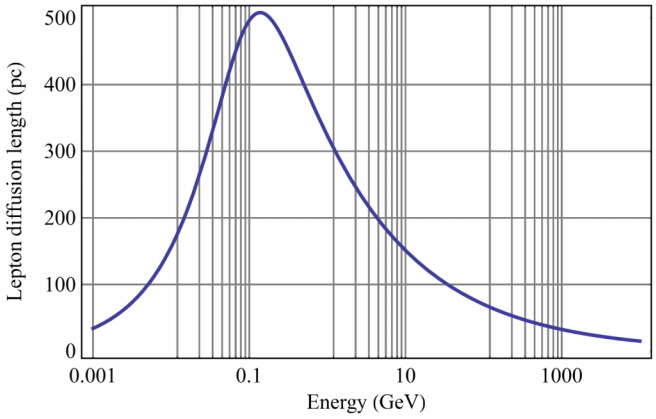

FIG. 13 (color online). The dependence of the lepton diffusion length l_D on the energy E. The magnetic field used is $B = 50\ \mu$G; the concentration is $n = 0.1$ cm^{-3}.

$$D(E) = D_0 \left(\frac{E}{E_0}\right)^{\delta}, \tag{B1}$$

with $D_0 = 10^{28}$ cm^2/s, $E_0 = 3$ GeV, and a Kolmogorov spectrum $\delta = 1/3$. The cooling time for leptons can be estimated as

$$\tau_{\text{loss}}(E) \sim \frac{E}{\dot{E}} = \frac{E}{b(E, \vec{r})}, \tag{B2}$$

where $b(E, \vec{r}) = b_{\text{ICS}} + b_{\text{sync}} + b_{\text{brem}} + b_{\text{Col}}$ [see Eqs. (8)–(11)]. After all necessary substitutions we obtained l_D dependence on the lepton energy E, which is shown in Fig. 13. For the magnetic field B and the concentration n we used the expected values for the M31 center, $\sim 50\ \mu$G and ~ 0.1 cm^{-3}, respectively. These parameter values were justified the Sec. II. As we can see in Fig. 13, the lepton diffusion path over the relevant range of energies does not exceed ~ 500 pc. Our emitting region, which we capture by our ROI with angular radius $\alpha \approx 5'$, would have the form of the cylinder with the radius $\rho_{\max} \approx \alpha d \approx 1100$ pc. Thus, the smallest size of the emitting region is about 2 times larger than the diffusion length of leptons in the M31 center. It means, in turn, that the leptons do not have enough time to migrate significantly and escape from the emitting volume before they cool down and discontinue radiation. Also taking into account the fact that the majority of total radiation flux due to DM annihilation is formed in the very central region, we can conclude that inclusion of the spatial diffusion in our calculations should not affect our results significantly. And neglecting by the diffusion is an acceptable approximation in our

computation procedure. Such a conclusion is in general agreement with the work [10] where the similar procedure of constraints derivation was conducted for the MW. However, since the spatial scale of the emitting volume and the lepton diffusion path do not differ drastically, we will allow an opportunity to include the diffusion in our calculations in a future work in order to improve the accuracy of our results.

[1] G. Bertone, *Particle Dark Matter: Observations, Models and Searches* (Cambridge University Press, Cambridge, England, 2010).
[2] J. L. Feng, M. Kaplinghat, and H.-B. Yu, Phys. Rev. D **82**, 083525 (2010).
[3] A. Geringer-Sameth and S. M. Koushiappas, Phys. Rev. Lett. **107**, 241303 (2011).
[4] J. Lavalle *et al.*, Astron. Astrophys. **450**, 1 (2006).
[5] M. Fornasa, M. Taoso, and G. Bertone, Phys. Rev. D **76**, 043517 (2007).
[6] M. Regis and P. Ullio, Phys. Rev. D **78**, 043505 (2008).
[7] http://lambda.gsfc.nasa.gov/.
[8] E. Corbelli, S. Lorenzoni, R. Walterbos, R. Braun, and D. Thilker, Astron. Astrophys. **511**, A89 (2010).
[9] S. Colafrancesco, S. Profumo, and P. Ullio, Astron. Astrophys. **455**, 21 (2006).
[10] E. Borriello, A. Cuoco, and G. Miele, Phys. Rev. D **79**, 023518 (2009).
[11] M. Longair, *High Energy Astrophysics* (Cambridge University Press, Cambridge, England, 2011).
[12] K. Ferrière, W. Gillard, and P. Jean, Astron. Astrophys. **467**, 611 (2007).
[13] http://www.marcocirelli.net/PPPC4DMID.html.
[14] M. Cirelli, G. Corcella, A. Hektor, G. Hütsi, M. Kadastik, P. Panci, M. Raidal, F. Sala, and A. Strumia, J. Cosmol. Astropart. Phys. 03 (2011) 051.
[15] P. Ciafaloni, D. Comelli, A. Riotto, F. Sala, A. Strumia, and A. Urbano, J. Cosmol. Astropart. Phys. 03 (2011) 019.
[16] J. F. Navarro, C. S. Frenk, and S. D. M. White, Astrophys. J. **490**, 493 (1997).
[17] A. W. Graham, D. Merritt, B. Moore, J. Diemand, and B. Terzić, Astron. J. **132**, 2701 (2006).
[18] V. Springel, J. Wang, M. Vogelsberger, A. Ludlow, A. Jenkins, A. Helmi, J. F. Navarro, C. S. Frenk, and S. D. M. White, Mon. Not. R. Astron. Soc. **391**, 1685 (2008).
[19] J. J. Geehan, M. A. Fardal, A. Babul, and P. Guhathakurta, Mon. Not. R. Astron. Soc. **366**, 996 (2006).
[20] M. Kamionkowski, S. M. Koushiappas, and M. Kuhlen, Phys. Rev. D **81**, 043532 (2010).
[21] E. Borriello, G. Longo, G. Miele, M. Paolillo, B. B. Siffert, F. S. Tabatabaei, and R. Beck, Astrophys. J. Lett. **709**, L32 (2010).
[22] A. Fletcher, E. M. Berkhuijsen, R. Beck, and A. Shukurov, Astron. Astrophys. **414**, 53 (2004).
[23] R. M. Crocker, D. I. Jones, F. Melia, J. Ott, and R. J. Protheroe, Nature (London) **463**, 65 (2010).
[24] R. Beck, Space Sci. Rev. **166**, 215 (2012).
[25] P. Hoernes, R. Beck, and E. M. Berkhuijsen, in *The Central Regions of the Galaxy and Galaxies*, edited by Y. Sofue, Proceedings of the 184th Symposium of the International Astronomical Union, Kyoto, Japan, 1997 (Kluwer, Dordrecht, 1998), Vol. 184, p. 351.
[26] M. Haverkorn and V. Heesen, Space Sci. Rev. **166**, 133 (2012).
[27] R. P. van der Marel and M.-R. L. Cioni, Astron. J. **122**, 1807 (2001).
[28] A. S. Cohen, W. M. Lane, W. D. Cotton, N. E. Kassim, T. J. W. Lazio, R. A. Perley, J. J. Condon, and W. C. Erickson, Astron. J. **134**, 1245 (2007).
[29] R. B. Rengelink, Y. Tang, A. G. de Bruyn, G. K. Miley, M. N. Bremer, H. J. A. Röttgering, and M. A. R. Bremer, Astron. Astrophys. Suppl. Ser. **124**, 259 (1997).
[30] J. J. Condon, W. D. Cotton, E. W. Greisen, Q. F. Yin, R. A. Perley, G. B. Taylor, and J. J. Broderick, Astron. J. **115**, 1693 (1998).
[31] J. J. Condon, J. J. Broderick, G. A. Seielstad, K. Douglas, and P. C. Gregory, Astron. J. **107**, 1829 (1994).
[32] F. Bonnarel, P. Fernique, O. Bienaymé, D. Egret, F. Genova, M. Louys, F. Ochsenbein, M. Wenger, and J. G. Bartlett, Astron. Astrophys. Suppl. Ser. **143**, 33 (2000).
[33] R. Trotta, Contemp. Phys. **49**, 71 (2008).
[34] A. Tamm, E. Tempel, P. Tenjes, O. Tihhonova, and T. Tuvikene, Astron. Astrophys. **546**, A4 (2012).
[35] R. M. Crocker, N. F. Bell, C. Balázs, and D. I. Jones, Phys. Rev. D **81**, 063516 (2010).
[36] E. Casuso and J. E. Beckman, Astron. J. **139**, 1406 (2010).
[37] G. Rybicki and A. Lightman, *Radiative Processes in Astrophysics* (WILEY-VCH Verlag GmbH, Weinheim, 2004).